GDCh Research Article Angewandte International Edition Chemie www.angewandte.org

How to cite: *Angew. Chem. Int. Ed.* **2025**, *64*, e202415436
doi.org/10.1002/anie.202415436

*Aqueous Aluminium-Ion Batteries*

# Strengthen Water O–H Bond in Electrolytes for Enhanced Reversibility and Safety in Aqueous Aluminum Ion Batteries

*Z. Zhao, Z. Zhang, W. Wang, T. Xu, and X. Yu**

**Abstract:** Aqueous aluminum-ion batteries present a promising prospect for large-scale energy storage applications, owing to the abundance, inherent safety, and the high theoretical capacity of aluminum. However, their voltage output and energy density are significantly hindered by challenges such as complex hydrogen evolution and uncontrollable solvation reactions. In this work, we demonstrate that water decomposition is restrain by increasing the electron density of water protons and increasing the dissociation energy of $H_2O$ through robust dipole interactions with highly polar dimethylformamide (DMF) molecules. Moreover, the incorporation of dimethyl methylphosphonate (DMMP) flame retardant effectively addresses the flammability risk arising from a substantial presence of organic additives The in-depth study with experimental and theoretical simulations reveals that the water-poor solvation structure with reduced water activity is achieved, which can (i) effectively mitigate undesired solvated $H_2O$-mediated side reactions on the Al anode; (ii) boost the de-solvation kinetics of $Al^{3+}$ while preventing cathode structural distortion; (iii) reduce the flammability of hybrid electrolytes. As a proof of concept, the Al//$Al_xMnO_2$ full cell employing a hybrid electrolyte demonstrate enhanced stability (deliver 335 mAh $g^{-1}$ while retaining 71 % capacity for 400 cycles) compared to those with pure electrolyte.

## Introduction

In the pursuit of advancing wind and solar energy, the imperative demand for efficient energy storage aligns with the promising application potential of aluminum ion batteries. Their allure is derived from inherent attributes such as safety, cost-effectiveness, the crust's abundance, and environmental compatibility.[1] Despite these merits, aqueous aluminum ion batteries (AAIBs) confront challenges including a limited electrochemical stability window (ESW), Al anode corrosion, and cathode material dissolution.[6] The electrolyte, due to water's constrained ESW, emerges as a pivotal factor influencing AAIBs performance. Exceeding an overvoltage threshold of 1.23 V results in water decomposition and gas generation during the cycle, a consequence of the narrow ESW of water.[8] The prevalence of $H_3O^+$ in weakly acidic electrolytes induces Al electrode corrosion, compromising the reversibility of aluminum (Al) electrodes. The suboptimal coulombic efficiency (CE) of Al ions at the electrode/electrolyte interface contributes to uneven Al deposition, profoundly impacting AAIB longevity. Additionally, multiple Al intercalations/extractions cause active material loss and swift capacity decline in the aqueous electrolyte, owing to structural collapse.[10]

Mitigating these challenges involves two primary strategies: Al electrode interface modification and electrolyte engineering.[6, 12] Despite encountering complexities such as intricate material preparation and escalating costs, electrolyte engineering distinguishes itself for its commercial viability. This is achieved by integrating functional additives to inhibit aluminum metal corrosion and hydrogen evolution. Within the realm of electrolyte engineering for aqueous metal batteries, two prominent strategies are highly rated: optimizing the solvent sheath structure of metal ions and enhancing O–H bonds in water to augment thermodynamic stability.[14] Leveraging metal salt in a concentrated "water-in-salt" electrolyte mitigates the metal ions ($M^+$)–$H_2O$ interaction, eliminating $H_3O^+$ and maintaining a neutral pH near 7.[16] Nevertheless, studies reveal that elevated concentrations of aluminum trifluoromethanesulfonate ($Al(OTf)_3$) weaken the $Al^{3+}$–$H_2O$ interaction, hastening aluminum salt hydrolysis.[18] Our group's innovative work introduces polar pyridinetricarboxylic acid into $Al(OTf)_3$ to optimize solvation structure, ensuring AAIBs cycle stability over 1000 hours.[19] However, the potential ionization of free water underscores the significance of reinforcing O–H bonds to comprehensively suppress side reactions. Common organic solvents, including trimethyl phosphate, N-methylpyridone, ethylene glycol and propylene carbonate, are incorporated into aqueous solutions to impede water decomposition.[20] This intervention operates through a mechanism aimed at disrupting hydrogen bonds among water molecules, thereby restraining water activity within the solvation sheath. Given the flammability of most electrolytes with organic additives, AAIBs pose safety risks. As research on AAIBs is in its nascent stage, developing synergistic strategies to strengthen O–H bonds in water, while concurrently preventing electrolyte combustion, presents a persistent and significant challenge.

Here, we propose enhancing the electron density of $H_2O$ protons to strengthen the electrostatic attraction between

[*] Z. Zhao, Z. Zhang, W. Wang, T. Xu, Dr. X. Yu
Department of Materials Science, Fudan University
Shanghai 200433 (China)
E-mail: yuxuebin@fudan.edu.cn

O–H bonds in $H_2O$, thereby suppressing the reactivity of $H_2O$ in AAIBs. The choice of dimethylformamide (DMF) as an additive from its high polarity, excellent compatibility, high electrochemical stability, featuring an electron-rich C=O moiety. Besides, the oxygen and nitrogen atoms in DMF possess lone pairs of electrons capable of coordinating with $Al^{3+}$ to form a stable complex. In comparison to a pure $H_2O$ solvent, the thermodynamics of water decomposition in a composite electrolyte are less favorable. By restricting the activity of $H_2O$, we can mitigate undesired hydrogen evolution resulting from water decomposition and other unwanted side reactions. Furthermore, as a flame-retardant additive, dimethyl methylphosphonate (DMMP) not only significantly reduces the combustibility of the mixed electrolyte but also leverages its electron-rich P=O moiety to interact with solvated water. This characteristic makes DMMP an effective flame retardant. Through this approach, we not only diminish the combustibility of the electrolyte but also modulate the activity of water, thereby reducing the occurrence of water decomposition reactions (Figure 1a). This contributes to improving the performance and safety of AAIBs. As a result, the Al anodes in the as-synthesized electrolyte exhibit superior $H_2O$ decomposition-free Al plating/stripping behaviours, with remarkably stable overpotential, for more than 700 h. The excellent electrochemical performances enable the Al–Mn AAIBs assembled with Al plate and $Al_xMnO_2$ cathode to deliver a high specific capacity with an extremely low-capacity delay rate of 0.007 % per cycles for 400 cycles. This foundational comprehension unveils a novel pathway for the effective harnessing of aluminum in advanced energy storage devices, with the prospect of extending its application to other multivalent cations frequently hindered by severe solvation reactions.

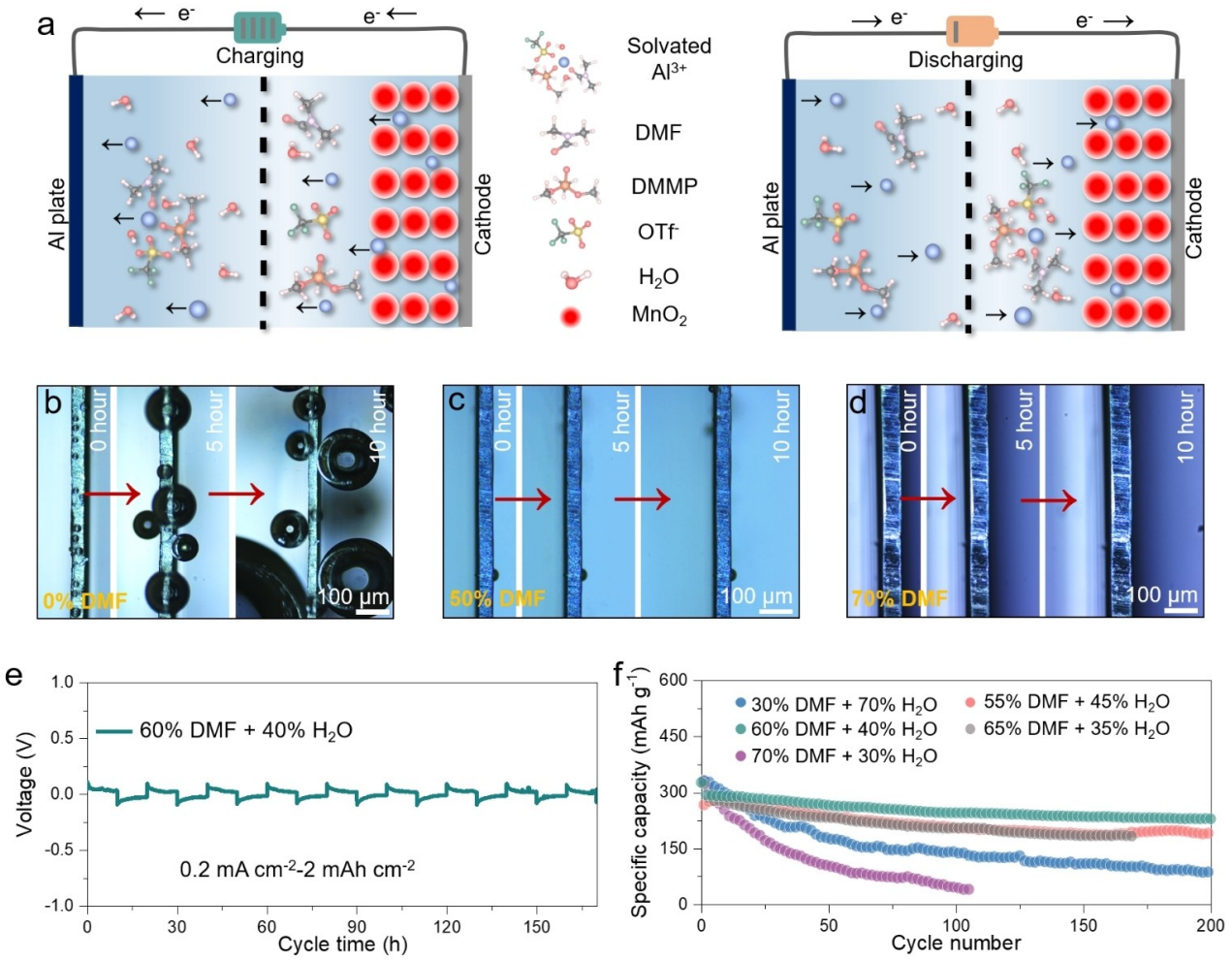


***Figure 1.*** Solvation structure and water O–H bond characterization in AE and HE. a) Schematic illustrations of the electrochemical mechanism of HE. b–d) Optical images of Al deposition on the negative side of Al//Al symmetric cells recorded in situ by an optical microscope system under 1 m $Al(OTf)_3$ with different DMF. e) Cycling performance of Al//Al cells using 1 m $Al(OTf)_3$ with 60 % DMF + 40 % $H_2O$. f) Cycling performance of Al//$MnO_2$ cells using 1 m $Al(OTf)_3$ with different DMF concentration.

## Results and Discussion

**Components of electrolyte**. Electrolyte design, guided by three fundamental tenets, unfolds as follows: i) exclusion of non-energy storage solutes from electrochemical processes; ii) optimization of carrier de-solvation kinetics to achieve superior performance; and iii) prioritization of environmental friendliness and non-flammability. Recognizing the profound influence of water content on battery electrode performance, our preliminary experiments aimed to investigate the optimal utilization of DMF. In this context, we introduced 1 m $Al(OTf)_3$ into mixed solvents with varying DMF/$H_2O$ volume percentages to formulate diverse electrolyte blends. Through in situ monitoring of gas evolution at the interface between Al and electrodes in Al//Al symmetric cells, it was found that when the volume fraction of DMF exceeds 50 %, the gas production from $H_2O$ decomposition at the Al electrode interface is successfully suppressed (Figure 1b–d and Figure S1). Subsequently, a systematic exploration of various electrolytes was conducted to assess their impact on the cyclic stability of Al//Al symmetric cells and Al//$MnO_2$ full batteries, leading to the identification of the optimal electrolyte formulation. In the mixed electrolyte, when the addition amount of DMF is between 55 % and 70 %, the Al//Al symmetric battery shows satisfactory cycle stability during the deposition/stripping process over 180 hours (Figure 1e and Figure S2). To efficiently determine the optimal DMF addition ratio in the mixed electrolyte, the Al//$MnO_2$ full batteries were assembled using the same batch of hydrothermally synthesized $MnO_2$ cathode materials, paired with Al anodes. And the $MnO_2$ electrode demonstrated superior cyclic stability over 200 cycles when the ratio of DMF was 60 % (Figure 1f).

Nevertheless, being a flammable organic solvent, the introduction of abundant DMF significantly heightens the flammability risk within the mixed electrolyte.[25] To mitigate this safety concern, we conducted further investigations into the utilization of DMMP within the DMF/DMMP mixture. Illustrated in Figure 2a, the addition of 10 % DMMP notably diminished the combustion intensity of the soaked separator. Even with a reduced volume ratio of DMMP to 12.5 %, residual black ash persisted on the slightly burned membrane surface (Figure S3b). With the introduction of 14.29 % DMMP, the flammability of the mixed solution was entirely eradicated (Figure 2b). Furthermore, experimental investigations into the concentration of DMMP addition revealed that complete elimination of flammability in the mixed solution is achieved when the DMMP addition reaches 9.1 % (Figure 2d). Consequently, the volume ratio of DMF/DMMP/$H_2O$ was optimized to 6:1:4. Within this formulation, the mixed solution containing 1 m $Al(OTf)_3$ is denoted as HE, while the aqueous solution with 1 m $Al(OTf)_3$ is labeled as AE.

Upon dissolution of aluminum salts, such as $Al(OTf)_3$, the pH undergoes a noteworthy decrease from approximately 7 in pure water to ca. 3.3 in 1 m $Al(OTf)_3$ aqueous solution (Figure S4). This acidification arises due to the interaction between $Al^{3+}$ and water molecules, prompting ionization. The electric field generated by $Al^{3+}$ exerts a force on water molecules, inducing electron transfer from coordinated $H_2O$ to the vacant orbitals of $Al^{3+}$. This process significantly attenuates the O–H bonds within $H_2O$ molecules and fosters hydrogen evolution.[27] Figure S5 shows the Raman spectra of the three electrolytes (1 m, 2 m and 3 m $Al(OTf)_3$ electrolyte) in the range of 750–790 $cm^{-1}$ ($–CF_3$) and 1000–1090 $cm^{-1}$ ($–SO_3$) at room temperature.[29] With increasing $OTf^-$ concentration, there is a noticeable blue shift observed in the $–CF_3$ and $–SO_3$ peak of the electrolyte, demonstrating the bending and stretching of C–F and S–O. The unstable bonding between $Al^{3+}$ and $OTf^-$, caused by the bending and stretching of functional groups, results in the destruction of the structure. Consequently, $Al^{3+}$ and $H_2O$ form transient bonds, leading to the creation of a dynamic octahedral solvation structure, accompanied by instantaneous electrostatic hydrolysis of the $Al–OH_2$ ligand. The microscopic solvation process of particles in $Al(OTf)_3$ solution is shown in Figure 2e–g. Initially, $Al^{3+}$ and six $H_2O$ randomly combine to form the inner sheath. Due to the non-fixed bond between $Al^{3+}$ and $H_2O$, $H_2O$ frequently escapes and associates with other particles (Figure 2e). With a +3 charge and small ionic radius, the $Al^{3+}$ exhibits an exceptionally high charge density, resulting in a strong electrostatic attraction toward surrounding molecules.[31] This interaction is particularly pronounced with polar water molecules, where the oxygen atoms carry a partial negative charge and the hydrogen atoms a partial positive charge. The attraction between $Al^{3+}$ and the water molecule dipoles leads to a highly dynamic solvation environment. Upon dissolving aluminum salts in water, $Al^{3+}$ readily coordinates with the oxygen atoms of water molecules through these intense electrostatic interactions. The $Al^{3+}$ ion, with its simplified electronic configuration of [Ne] and vacant *3 s* and *3p* orbitals, tends to adopt coordination environments that minimize energy.[32] In aqueous solutions, $Al^{3+}$ typically coordinates with six water molecules, forming a highly symmetric octahedral structure. This six-coordinate geometry optimizes charge neutralization, reduces electrostatic repulsion, and efficiently utilizes space, positioning the water molecules at the vertices of a regular octahedron with equal bond lengths and 90° angles between adjacent ligands. This configuration achieves the lowest total energy for the system. A single crystal of the $Al^{3+}$ solvation structure in a pure $Al(OTf)_3$ solution was obtained by the slow evaporation of the solvent. Figure S6 displays the refined single crystal X-ray diffraction (SC-XRD) results of this crystal. As illustrated in the magnified section of Figure S6, $Al^{3+}$ in solution is coordinated by six water molecules, forming the $[Al(H_2O)_6]^{3+}$ complex.

The high positive charge of $Al^{3+}$ creates a strong electrostatic attraction, causing a redistribution of electron density in the O–H bond of nearby water molecules. This polarization effect enhances the interaction between $Al^{3+}$ and the water molecules, ultimately leading to the cleavage of the O–H bond and the rapid formation of $H^+$ and $OH^-$.[33] The resulting hydrolysis process is instantaneous, swiftly bringing the system to equilibrium. To study this phenomenon, $^1H$ NMR spectroscopy is used to examine changes in the hydrogen atomic environment in solutions

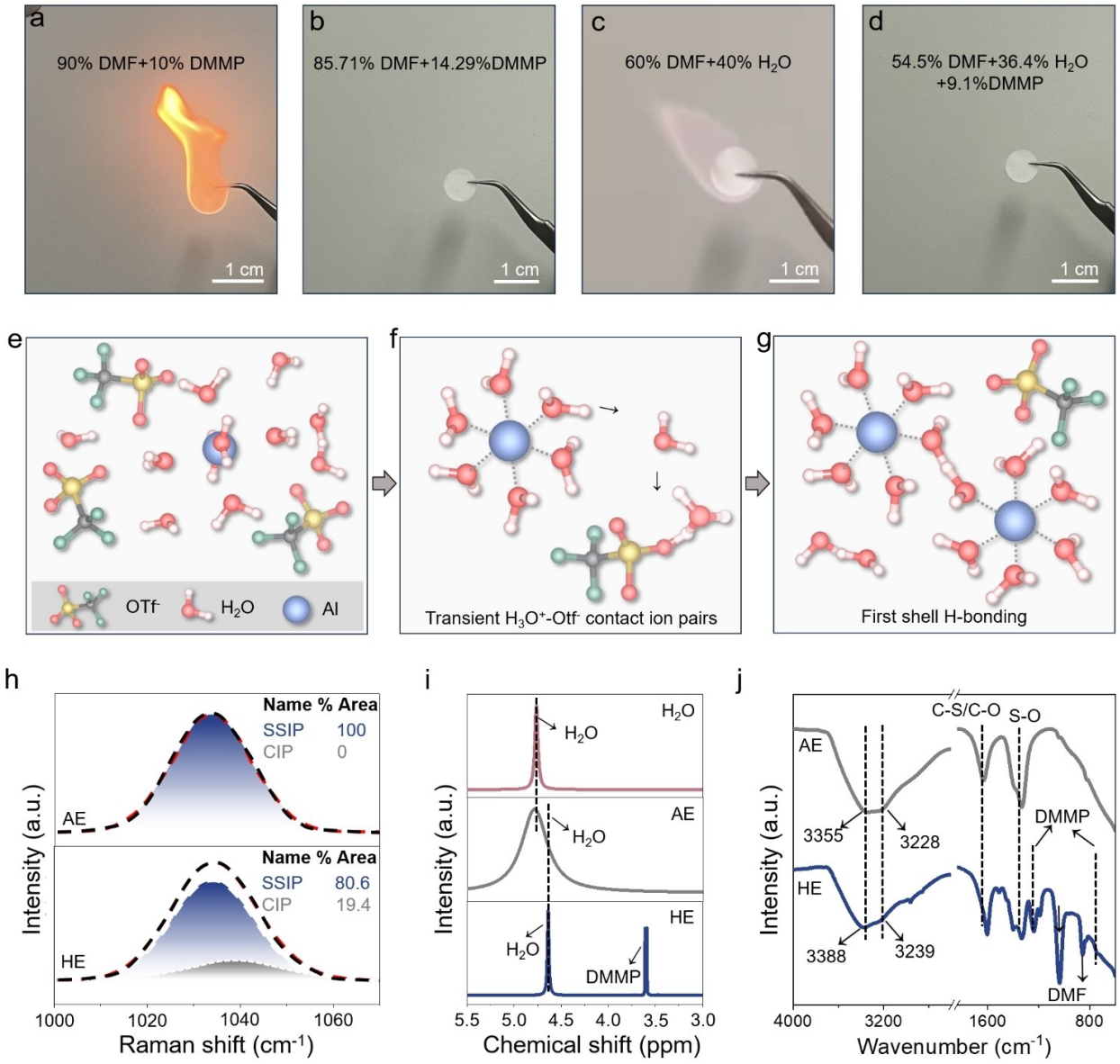


***Figure 2.*** Digital images of combustion test for 1 m $Al(OTf)_3$ solutions with the solvent of a) DMF/DMMP = 9:1, b) DMF/DMMP = 6:1, c) DMF/$H_2O$ = 6:4, d) DMF/$H_2O$/DMMP = 6:4:1. e–g) Solvation in $Al(OTf)_3$ solution. h) Raman spectra for AE and HE. i) $^1H$ NMR spectra of $H_2O$ in water, AE and HE. j) FTIR spectra for AE and HE.

containing $H_2O$ and $Al(OTf)_3$. Compared to pure water, the Al–$OH_2$ ligands in the $Al(OTf)_3$ solution show a chemical shift to a higher field due to the dissociation of $H^+$ and the integration of $OH^-$ into the hydrogen bond network (Figure 2i). The transient hydrolysis of $Al(OTf)_3$ creates various coordination environments, leading to broadening of the $^1H$ NMR signal as hydrogen atoms experience different local magnetic fields within a short time frame.[34]

In acidic aqueous solutions, protons ($H^+$) rapidly ionize and migrate between water molecules through the Grotthuss mechanism, leading to the formation of transiently hydrated species like $H_3O^+$. In the strongly acidic $Al(OTf)_3$ electrolyte, protons are likely to coordinate with two water molecules simultaneously, resulting in the formation of more complex hydrated structures. In this arrangement, the proton is shared between the oxygen atoms of two adjacent water molecules, rather than being localized to one. This equal sharing of the proton forms a Zundel cation ($H_5O_2^+$) (Figure 2f).[35] To confirm the presence of Zundel cations in $Al(OTf)_3$ electrolytes, Raman spectroscopy was performed in the 1500 to 4000 $cm^{-1}$ range, enabling the identification of distinct vibrational features. Figure S7 shows that $H_5O_2^+$ cations arise from the hydration of dissociated protons with two water molecules, with the remaining water largely existing as monomers. The linear Raman spectrum shows the distinctive vibrational signature of the $H_5O_2^+$ cation. In the infrared spectrum of the $Al(OTf)_3$ electrolyte, a significant O–H bending absorption peak corresponding to

$H_5O_2$ was detected, along with a weaker O–H vibration peak of free water at 3480 $cm^{-1}$. Conversely, the Raman spectrum of pure water lacked vibration peaks between 1200–1800 $cm^{-1}$, as the neutral electrolyte environment is unfavorable for Zundel cation formation. Instead, a strong O–H vibration peak at 3470 $cm^{-1}$ indicated that protons in pure water predominantly exist as $H_3O^+$ or free water molecules. As a hybrid of covalent and hydrogen bonds, the Zundel cation is extremely unstable in aqueous solutions. When $H_2O$ molecules surpass the effective range of $Al^{3+}$, they will bind with $OTf^-$ to create $H_3O$–OTf.[18] Metal-bound water ligands can release protons, leading to strong delocalization between sheaths. Protons rapidly shuttle back and forth between hydroxyl groups, establishing coupling between adjacent aluminum solvation shell sheaths through tight hydrogen bonds (Figure 2g). As a polar organic solvent, DMF is known for its strong hydrogen bond accepting capabilities.[36] The C=O and C–N groups in DMF facilitate the formation of hydrogen bonds with water molecules. Specifically, the oxygen atoms in DMF engage with the hydrogen atoms of $H_2O$, thereby disrupting the original hydrogen bond network between water molecules. This interaction weakens or even disrupts the hydrogen bonding network within the aqueous solution. Notably, the hydrogen bonds formed between DMF and water are stronger than those between water molecules, leading to a significant disruption of the hydrogen bond network in the aqueous electrolyte (Figure S8).

**Optical characterization**. To prove the inhibitory effect of polar DMF and DMMP additives on the reactivity of $H_2O$ in AE electrolyte, various experimental characterizations combined with theoretical calculations were conducted. Different spectral analyses, including nuclear magnetic resonance (NMR), Fourier transform infrared spectroscopy (FTIR), and Raman spectroscopy, were first employed on AE and HE electrolytes. The Raman spectrum illustrates a discernible shift in the signal corresponding to v($OTf^-$) vibration to a higher wavenumber (from 1033.4 $cm^{-1}$ in AE to 1034.5 $cm^{-1}$) upon the addition of DMF and DMMP (Figure 2h). Notably, distinct differences in the Raman spectra between AE and HE are observed in the range of 1043.8–1058.2 $cm^{-1}$ (Figure S9). The addition of DMF and DMMP results in a noticeable shift of the signal corresponding to the v($OTf^-$) vibration to higher wavenumbers (from 1033.8 $cm^{-1}$ in AE to 1036.4 $cm^{-1}$). Concurrently, the full width at half maximum of the SSIP vibration peak significantly decreases (from 23.8 $cm^{-1}$ in AE to 21.2 $cm^{-1}$).This evolving trend signifies a transformation in the solvation structure of $Al^{3+}$ from pure solvent-separated ion pairs (SSIP) to the coexistence of SSIP and contact ion pairs (CIP).[37] Simultaneously, the vibration of v($H_2O$) in the range of 2800–4000 $cm^{-1}$ also experiences a slight forward shift in HE, demonstrating the presence of a robust intermolecular hydrogen bond between additives and water (Figure S10).[39]

The DMF/$H_2O$ ratio emerges as a pivotal determinant influencing the strengthening or weakening of hydrogen bonds. The effect on $H_2O$ molecules in HE is validated by the $^1H$ NMR spectrum.[40] In Figure 2i, the resonance of water protons at ca. 4.74 ppm in pure water undergoes broadening in AE, attributed to water molecules participating in solvation clusters. This broadening is induced by $Al^{3+}$ facilitating electron transfer from the water proton moiety to the vacant orbital of $Al^{3+}$. The reduction in electron density on water protons results in the loss of shielding effect on the $^1H$ nucleus, causing a downward shift in proton resonance frequency. Notably, water protons in HE exhibits a significant up-field shift of ca. 0.13 ppm, indicative of increased electron density compared to pure water and AE (Figure 2i). The electron-rich regions of DMF and DMMP, characterized by C=O and P=O groups, respectively, contribute to heightened electron density of water protons upon interaction with water. FTIR, being highly responsive to alterations in molecular dipole moments, serves as a valuable tool for assessing the impact of polar molecules on the O–H bonds of water. In AE, the absorbance band within the 2900–3700 $cm^{-1}$ range is associated with the O–H stretching vibration (Figure 2j).[41] Two peaks located at 3369 and 3207 $cm^{-1}$ are ascribed to O–H stretching from intermediate water and network water, respectively. It is found that these peaks undergo an obvious blue shift, implying a weakening of hydrogen bonds and a strengthening of O–H bonds. Furthermore, for HE, a red shift is observed in the C–O/C–S vibration of $OTf^-$, which may arise from the conjugation effect of the introduced C=O and other groups weaken the double bond nature of the original C–S/C–O, leading to a decrease in the absorption frequency.

**MD simulation**. In order to prove the inhibitory effect of polar DMF and DMMP additives on the reactivity of AE electrolyte water, molecular dynamics (MD) simulations were performed. The participation of organic solvents, namely DMF and DMMP, as well as $OTf^-$, in the formation of the solvation shell is evident from Figure S11. As illustrated in Figure 3a, the primary solvation shell (PSS) of $Al^{3+}$ in AE comprises six $H_2O$ molecules. Upon the introduction of DMF and DMMP, a portion of the $H_2O$ molecules in the PSS is replaced. By assessing the distribution of nearest neighbor molecules surrounding $Al^{3+}$, the average coordination number (ACN) and radial distribution function (RDF) for both systems were obtained (Figure 3a–c and Figure S12). Evidently, in the AE system, no anions are detected within the PSS of $Al^{3+}$. In the heterogeneous environment containing DMF and DMMP, the coordination number is ca. 6, encompassing 2.9 water molecules, 1.1 $OTf^-$ anions, 0.9 DMMP molecules, and 1.0 DMF molecule, realizing the successful formation of HE. The substitution of $H_2O$ molecules by additive ions in the heterogeneous environment is associated with low solvating capacity of the solvent. The impact of dielectric constant on the interaction between metal ions ($M^+$) and the solvent can be elucidated through classical physiochemical principles, that is

$$U_{M^+-solvent} = \frac{-1}{4\pi\varepsilon} \times \frac{q\mu cos\theta}{r^2}$$

$U_{M^+-solvent}$ is the interaction of $M^+$-solvent, $q$ is the charge number of the ion, $\mu$ is the dipole moment of the dipole, $\varepsilon$ is the dielectric constant, $r$ is the distance between

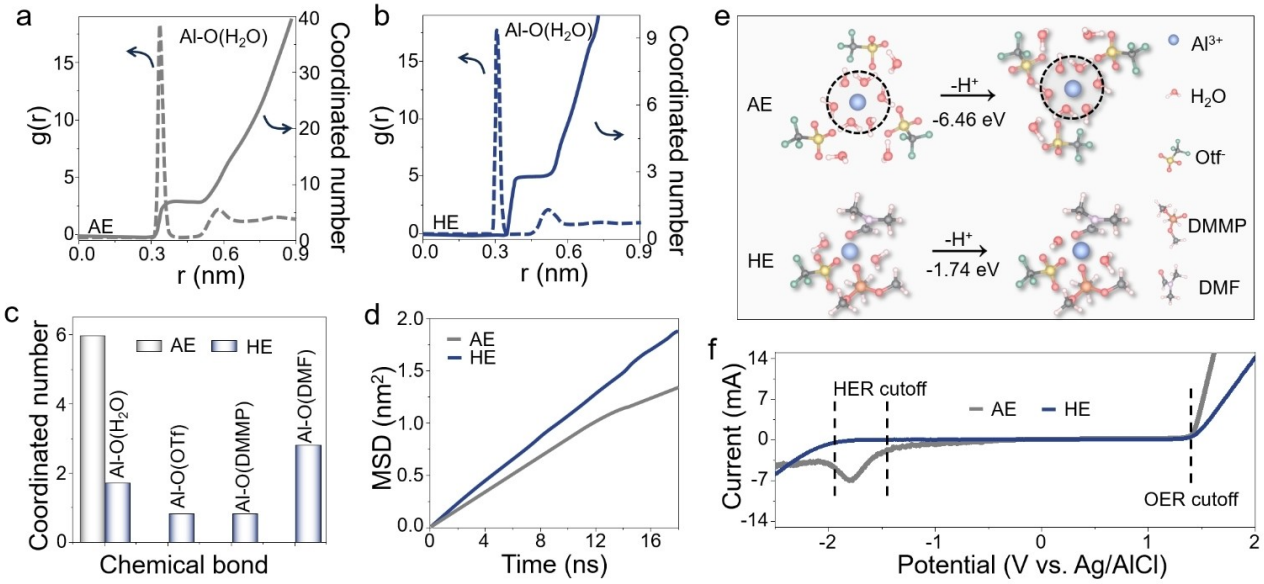


***Figure 3.*** The MD simulations, DFT calculations and electrochemical performance of Al anode in AE and HE. RDFs a) $Al^{3+}$–O pairs in AE and b) $Al^{3+}$–O pairs in HE. c) Coordination number of $Al^{3+}$ with different species in AE and HE. d) MSD as a function of time under AE and HE. e) Deprotonation ($H^+$ dissociation of water) energy from $Al^{3+}$ PSS of AE and HE calculated form density functional theory. f) LSV curves in AE and HE at 2 mV $s^{-1}$.

the ion and the dipole, and $\theta$ is the dipole angle. In HE, the incorporation of low-conductivity organic additives markedly diminishes the dielectric constant of the solvent, which leads to a pronounced attenuation of the interaction between $Al^{3+}$ and the solvent, thereby increasing the probability of anions entering the PSS of $Al^{3+}$ to form $[(Al^{3+})(H_2O)_{2.9}(OTf^-)_{1.1}(DMMP)_{0.9}(DMF)_1]$ CIP. The correlation between mean square displacement (MSD) and time can be used to evaluate the diffusion rate of $Al^{3+}$ under different electrolyte systems. For HE, the diffusion coefficient of $Al^{3+}$ shows a proportional increase with the slope of MSD versus time, suggesting that the revised PSS, to some extent, is helpful for transferring $Al^{3+}$ (Figure 3d).

**Density functional theory calculation**. Due to the addition of DMF/DMMP, $H_2O$ molecules display strengthened O–H bonds and exhibit increased resistance to decomposition. Density functional theory (DFT) calculations were subsequently conducted to investigate the deprotonation energy associated with the dissociation of $H^+$ and $H_2O$ within the $Al^{3+}$ PSS (Figure 3e). As evident from the simulation results, the dissociation of $H^+$ and $H_2O$ in the heterogeneous environment is significantly less favorable compared to the aqueous environment (−6.46 eV vs. −1.74 eV). The plating/stripping potential of $Al^{3+}$ was evaluated using an Al//Al symmetric cell (Figure 3f and Figure S13). In AE electrolyte, when the test voltage reaches −1.8 V, water undergoes reduction, leading to hydrogen evolution (a side reaction clearly manifested as a pronounced reduction peak in the LSV curve), which disrupts the deposition behavior of $Al^{3+}$ and significantly impairs battery performance. In contrast, by optimizing the composition of the HE electrolyte to strengthen the O–H bond in $H_2O$ and refine the solvation structure of $Al^{3+}$, the hydrogen evolution reaction is effectively suppressed, and $Al^{3+}$ deposition is better regulated. The addition of DMF/DMMP further mitigates HER near −1.8 V, thereby eliminating the corresponding peak in the LSV curve. As depicted in Figure 3f, in comparison to the AE, the HE demonstrates the ability to shift the onset potential of the hydrogen evolution reaction (HER) from −1.35 V to −1.93 V, suggesting that the altered solvation structure and O–H bonds in HE significantly suppresses the activity of the HER. To assess the corrosion current in the two electrolyte systems with and without DMF/DMMP, linear polarization tests were conducted (Figure S14). The corrosion current resulting from the addition of DMF/DMMP is 0.676 mA $cm^{-2}$ lower than that observed with pure $Al(OTf)_3$ (1.23 mA $cm^{-2}$), suggesting that these additives assist in mitigating water decomposition.

**Deposition and stripping of Al**. In Al//Ti batteries, the CE of Al//Ti batteries serve as a direct measure of charge utilization per cycle and provides insights into the desolvation of $Al^{3+}$ in the electrolyte. Figure 4a illustrates the stability and CE for Al//Ti cells employing AE and HE as the electrolyte at a current density of 0.2 mA $cm^{-2}$ and plating/stripping capacity of 0.2 mAh $cm^{-2}$. In the initial cycles, the deposition/stripping of Al on the Ti foil undergoes an interface restructuring phase, resulting in a relatively low CE. Over the subsequent 20 cycles, the Al//AE//Ti cell maintains a relatively stable CE, consistently exceeding 80 %. However, due to side reactions such as hydrogen evolution and corrosion, the CE experiences fluctuations, rapidly decreases in stability in subsequent cycles up to a short circuit. The Al//Ti cell in AE electrolyte exhibits

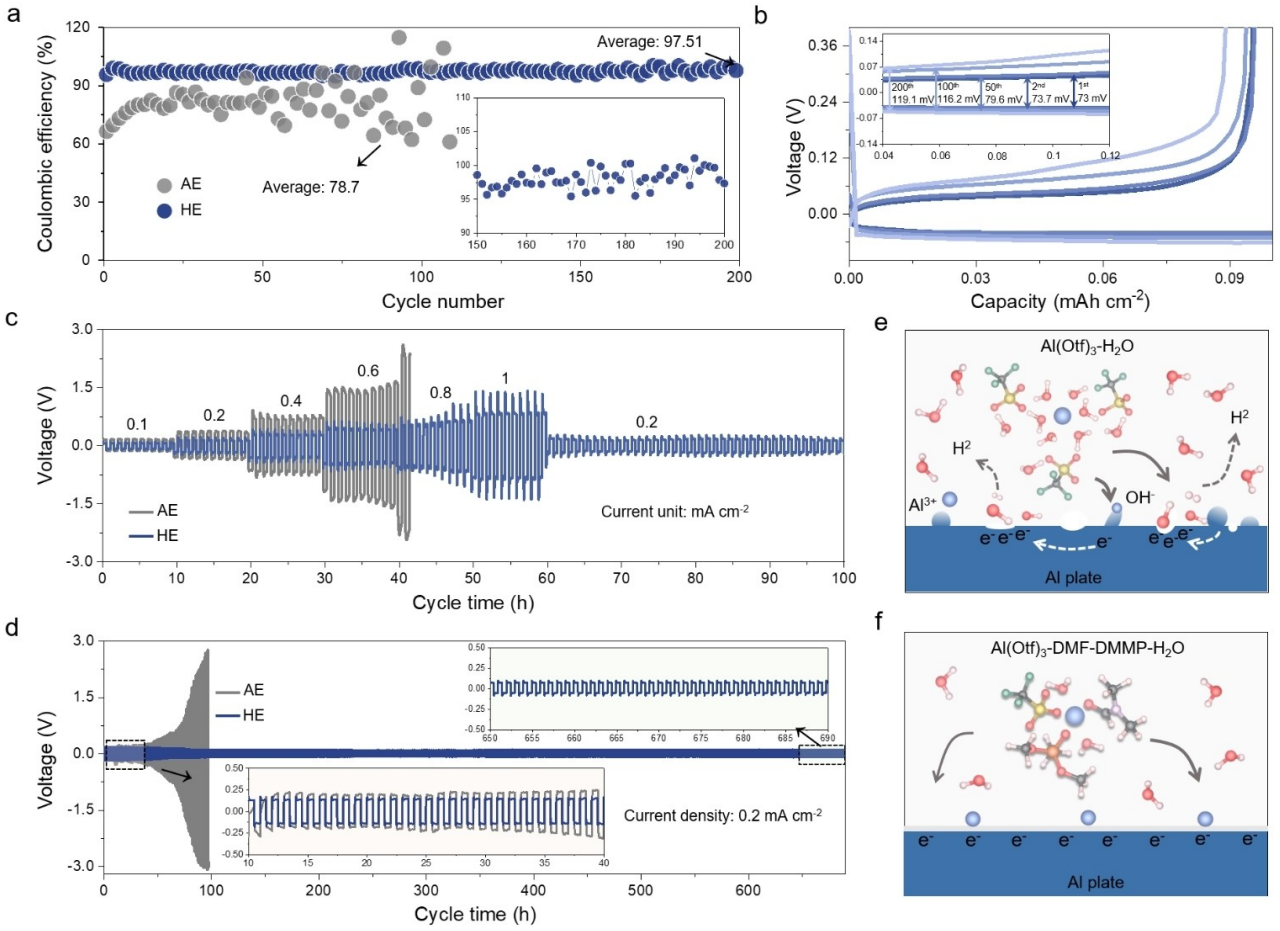


***Figure 4.*** Al deposition in AE and HE and corresponding protection mechanism study. a) Al plating/stripping Coulombic efficiency in AE and HE at 0.2 mA cm$^{-2}$ and 0.2 mAh cm$^{-2}$. b) Voltage profiles of Al plating/stripping processes at selected cycles in HE. c) Comparison of voltage profiles for Al symmetric cells in AE and HE electrolyte at different current densities for 1 h at each step. d) Galvanostatic cycling profiles of Al symmetric cells with AE and HE at 0.2 mA cm$^{-2}$–0.2 mAh cm$^{-2}$. The Scheme delineates distinct reaction processes of $Al^{3+}$ solvation structures in e) AE and f) HE systems and the corresponding interfacial interactions between the Al anode surface and the electrolyte.

undulatory voltage signals with a low average CE of approximately 78.7 %. In contrast, the Al//Ti cell using the HE electrolyte demonstrates a significant improvement in stability and reversibility for the Al anode. Notably, the battery reached a very high and stable Al plating/stripping efficiency within 5 cycles and maintained for over 200 cycles, with an average CE of 97.51 % (Figure 4a). This performance stands out as one of the best among all reported AAIBs. The use of the component solvent further confirms the generality of the DMF/DMMP additive in enhancing Al plating/stripping CE.

To investigate the reversibility of the $Al^{3+}$ deposition and stripping process and the stability of the electrode surface, electrochemical measurements were performed on a symmetrical cell consisting of two identical electrodes. Figure 4c illustrates the voltage curve of the pretreated Al symmetric cell (see the experiment section for details) undergoing Al deposition/stripping processes at various current densities in HE electrolyte, contrasting with the voltage curve of the symmetric cell employing AE electrolyte. The Al//HE//Al symmetrical cell has a steadily increasing hysteresis of 73, 135, 284, 428, 548 and 796 mV when the current density is increased from 0.1 to 0.2, 0.4, 0.6, 0.8, and 1 mA cm$^{-2}$. These hysteresis voltages are much lower than those in Al symmetric cells with AE electrolyte (~170, ~390, ~760, ~1600 and ~2390 mV). Although the introduction of DMF/DMMP slightly reduces the ionic conductivity and increases the interface resistance, the total resistance of the Al//Al symmetric cell in HE electrolyte is comparable to AE electrolyte (The reaction impedance ($R_{ct}$) value increases from 421.3 Ω in AE to 463.7 Ω in HE) due to the rapid charge transfer reactions (Figure S15). In order to assess the cyclic stability of Al stripping/plating in the electrolyte, the symmetrical cells were subjected to long cycles at high current densities of 0.2 and 0.5 mA cm$^{-2}$, and the results are shown in Figure 4d and Figure S16. The voltage curve of the Al//HE//Al cell did not show any significant voltage lag even after more than 700 hours during the long-term Al stripping/plating cycling measurement, which is in sharp contrast to those of the Al//AE//Al with much larger voltage hysteresis and fluctuation after 40 hours. Attractively, even employing a high current of 0.5 mA cm$^{-2}$ and a high capacity of

$0.5\,mA\,cm^{-2}$, the voltage distribution of the Al//HE//Al symmetrical cell showed no significant fluctuations in long-term cycling over 500 hours, except for the slight increase in overpotential from the initial 487 mV to 495 mV due to DMF/DMMP increases the electron density of water protons and inhibits water decomposition activity (Figure S13).

Given the occurrence of the $Al^{3+}$/Al solidification transition in a solvent-based medium, our study delved into investigating the influence of electrolyte solvent composition on the morphology of Al deposition. In the AE electrolyte, where $H_2O$ serves as the sole solvent and 1 m $Al(OTf)_3$ acts as the salt, the resulting Al deposition morphology is porous and irregular, lacking preferential orientation (Figure S17c and d), which is in stark contrast to the regular morphology observed in the case of HE. It demonstrates that the utilization of a DMF/DMMP/$H_2O$ hybrid solvent is pivotal for achieving uniform Al electroplating. In general, the crystal structure is decided by the relative growth rates among crystallites with different orientations. X-ray diffraction (XRD) analyses were conducted to assess the crystal structure of Al deposits following 25 cycles at a current density of $1\,mA\,cm^{-2}$–$1\,mAh\,cm^{-2}$ (Figure S18). The [220] peak of the Al electrode is the strongest after cycling in AE and HE for 50 h. The intensity ratios of the [220] peak to the [311] peak of AE and HE are 1.26 and 1.99, respectively, indicating that the [220] facet of Al deposits increases in HE (JCPDS Card No. 29–0914). Given the face-centered cubic lattice of Al metal (space group: *Fm-3 m*), it is speculated that the deposited Al is stacked perpendicularly along the *c* axis, resulting in the smooth surface observed in the SEM image (Figure S17e and f). To assess the stability of the Al electrode in HE electrolyte, three-dimensional contour images of the Al plate interface were acquired using laser microscopy (Figure S19). Uniform exfoliation of Al in HE was observed, and no granular protrusions were detected throughout the deposition process, which is consistent with the scanning electron microscopy (SEM) images of Al symmetric cells after cycling (Figure S17).

**Al electrode interface components**. The elemental composition of the contact surface was precisely determined through X-ray photoelectron spectroscopy (XPS) analysis, as illustrated in Figure S19 and S20. For the Al plate cycled in AE, strong signals appeared in the S *2p* and F 1s spectra, proving the side reaction products produced by the decomposition of the electrolyte at the Al plate interface during the cycling process (Figure S20).[42] It should be noted that the XPS results show that severe corrosion during the cycle destroyed the passivation layer on the contact surface of the Al electrode, causing part of the Al to be directly exposed to the electrolyte, exacerbating the inward corrosion of the Al electrode (Figure S21a and b). In contrast, the deposited Al surface under the HE owns no S, F and $Al^0$, indicating effective prevention of common by-reactions. The C 1s analysis of the Al electrode cycled in AE revealed the presence of $CO_3^{2-}$, C–O–C, C–S, and C–H bonds, suggesting the occurrence of a conversion reaction between the Al electrode, $H_2O$, and $OTf^-$ in the electrolyte (Figure S21c). Conversely, the absence of $-CF_2$ on the Al electrode cycled in HE indicates that the addition of DMF/DMMP effectively inhibits the decomposition of solvents. This inhibition is further supported by the S *2p* XPS spectrum, which identified decomposition products of $OTf^-$, including $SO_3$ and $S^{2-}$ species in the cyclic Al electrode (Figure S20a and b). To effectively detect the composition of the passivation layer of the Al electrode after cycling, in the revised manuscript we used secondary ion mass spectrometry to investigate the structural information of the passivation layer on the surface of the strip electrode. The organic components (such as $CF_2$) with minor inorganic $CO_3^{2-}$ species were detected on the cycled Al electrode, as evidenced by the secondary ion mass spectrometry in Figure S21. The $CF_2$ and S species arise from either of incomplete reduction products of $OTf^-$ or trace $Al(OTf)_3$ residue on Al surface, which is consistent with previous XPS results.[45] C–N bond-containing DMF in the electrolyte form an organic passivation layer on the electrode surface during the electrochemical process, enhancing electrode-electrolyte compatibility, reducing local current density, improving interface stability, thereby enhancing battery cycle life and stability. Additionally, the additive modulates $Al^{3+}$ deposition kinetics by altering its solvation structure and diffusion pathways, promoting deposition along the electrode interface. Therefore, the detection of C–N further underscores the involvement of DMF in the controlled deposition of $Al^{3+}$ at the interface.

The above theoretical calculations and experimental tests prove that the addition of DMF/DMMP additive suppress water decomposition by increasing the electron density of the water protons in the electrolyte, greatly improves the stability of Al deposition/stripping, and extends the service life of the battery. The mechanism of using DMF/DMMP additives to inhibit the Al–$H_2O$ solvation side reaction is concluded in Figure 4e and f. During the deposition process of $Al^{3+}$ ions, the Al solvation structure in the pure $Al(OTf)_3$ solution will generate a large number of active water molecules at the electron-rich interface as it moves toward the electrode, thus deriving a series of side reactions that endanger the normal deposition of carriers: (1) The strong coulombic interaction between solvated aluminum ions and surrounding water molecules creates a high-potential zone in the vicinity, accelerating the electron-driven hydrogen evolution during the aluminum deposition process; (2) After hydrogen evolution accumulates at the electrode interface, resulting in the corrosion of Al electrode and a gradual increase in pH values; (3) The $OH^-$ environment promotes the formation of a low-conductivity passivation layer of Al ions on the Al surface, hindering the deposition of aluminum electrodes and accelerating the decomposition of water; (4) Combined with the above reactions, uncontrollable solvation on the surface of the exposed aluminum electrode causes serious hydrogen evolution and corrosion problems, leading to the irreversible transformation process of Al/$Al^{3+}$ and the risk of battery bulging or even collapse. The introduction of polar DMF/DMMP into the electrolyte increasing the electron density of the water protons in the aluminum solvation sheath. This inhibits the solvation reaction at the electrode interface, as

more reactive $H_2O$ molecules are unable to obtain electrons for decomposition.

**Al//Al$_x$MnO$_2$ full cells**. In view of the superior electrochemical performance of HE electrolyte and Al pre-intercalated Al$_x$MnO$_2$ nanorods (Al$_x$MnO$_2$), the Al$_x$MnO$_2$ was used as the cathode and coupled with the pretreated Al plate (see the method for detail) material to demonstrate its practical application in Al ion full batteries (Figure S22).[37] Figure 5a shows the typical cyclic voltammetry (CV) curves of Al ion full batteries that are assembled with AE and HE electrolyte, i.e., Al//AE//Al$_x$MnO$_2$ or Al//HE//Al$_x$MnO$_2$. The Al//AE//Al$_x$MnO$_2$ and Al//HE//Al$_x$MnO$_2$ share identical anode and cathode materials, their voltametric behaviors diverge as a result of variations in the electrolyte composition. This discrepancy underscores the crucial role of DMF/DMMP in optimizing the deposition and stripping processes of aluminum, emphasizing its significance in influencing battery performance. By virtue of the optimized Al plating/stripping performances of DMF/DMMP enabling fast reaction kinetics of $Al^{3+}$ (de) intercalation in Al$_x$MnO$_2$, Al//HE//Al$_x$MnO$_2$ cells exhibit enhanced current density and positive shift in cathodic/anodic peak. As shown in Figure 5a, the anodic and cathodic peaks of the HE cell are 1.58 and 1.21 V, respectively, and the voltage difference is 370 mV (the scan rate is 0.15 mV s$^{-1}$). When substituting the electrolyte with AE, there was a notable increase in the voltage difference between the anodic and cathodic peaks, reaching ca. 710 mV.

To elucidate the electrochemical processes corresponding to the multiple reduction and oxidation peaks observed in Figure 5a, we have conducted ex situ XPS analysis of the Al$_x$MnO$_2$ cathode at various electrochemical states. As shown in Figures S23, XPS analysis reveals the co-existence of Mn in both +4 and +2 states within the Al$_x$MnO$_2$ electrode during discharge. With increasing discharge depth, there is a progressive increase in the proportion of $Mn^{2+}$ (Figure S23a). Upon recharging the AAIBs to 1.7 V, the $Mn^{2+}$ in the Al$_x$MnO$_2$ cathode is largely re-oxidized to

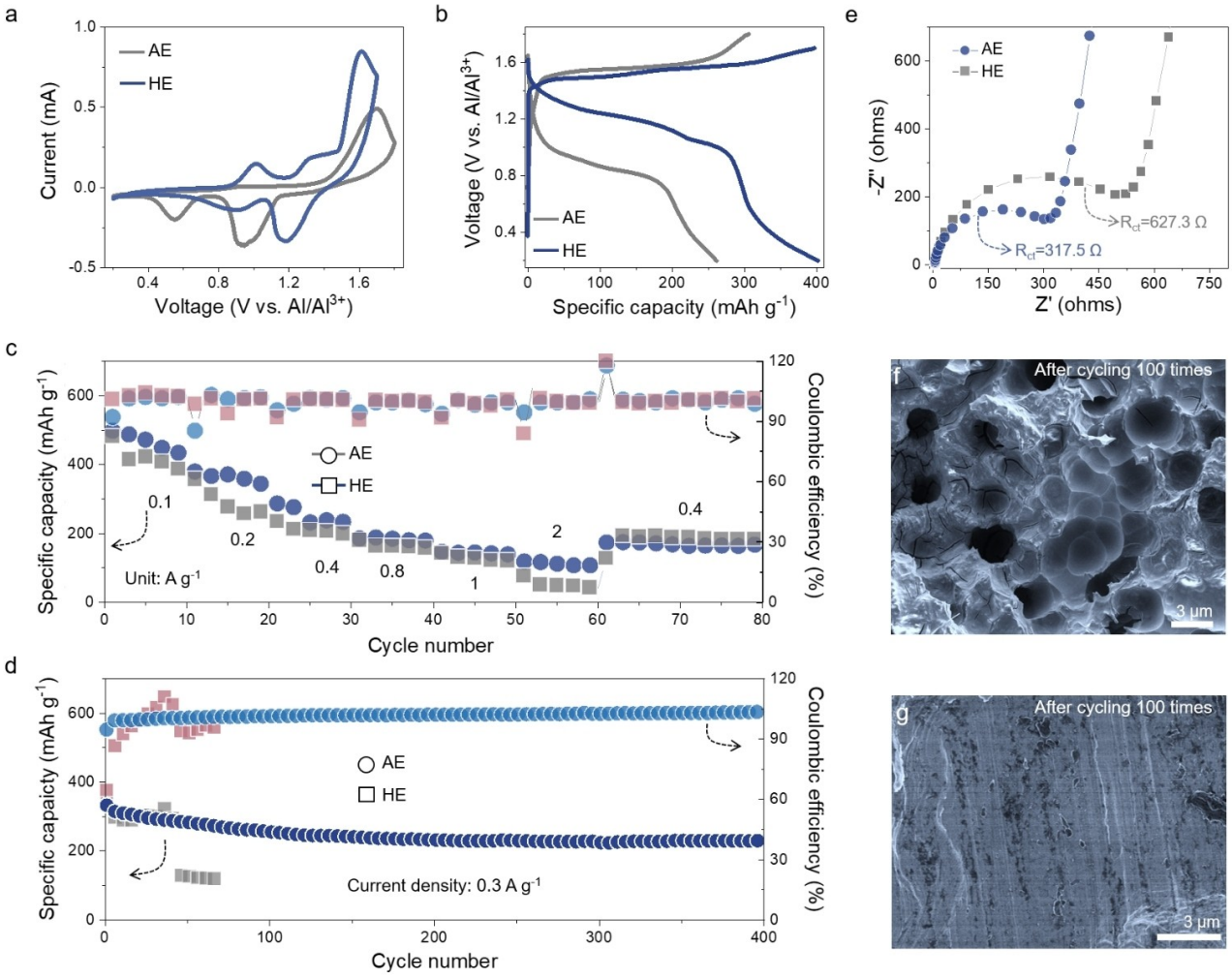


***Figure 5.*** Performance comparison of Al//Al$_x$MnO$_2$ full cells between AE and HE electrolytes. a) Typical CV curves for Al//Al$_x$MnO$_2$ full batteries in AE and HE electrolyte. Scan rate: 0.15 mV s$^{-1}$. b) GCD curves at 0.1 A g$^{-1}$, c) rate capability comparison and d) cycling stability comparison at 0.3 A g$^{-1}$ of Al//Al$_x$MnO$_2$ cells in AE and HE (the square is HE and the circle is AE). e) Impedance spectra (Nyquist plots) of Al//Al$_x$MnO$_2$ cells in AE and HE. Morphology for Al foil following working in f) AE and g) HE for 100 cycles.

$Mn^{4+}$, leaving only trace amounts of $Mn^{2+}$, indicating excellent electrochemical reversibility of the synthesized $Al_xMnO_2$ material (Figure S23b and c). Additionally, the Al *2p* XPS spectrum of the $Al_xMnO_2$ cathode (Figure S23c) clearly exhibits reversible changes in the Al *2p* signal during cycling, closely mirroring the behavior observed in the Mn *2p* spectrum, which further supports the material's robust reversibility. Consequently, the reduction peaks at 1.2 V and 0.9 V in Figure 5a are associated with the two-step intercalation of $Al^{3+}$ and the reduction of $Mn^{4+}$ in the $Al_xMnO_2$ cathode. The oxidation peaks at 1.0 V and 1.6 V during the charge process correspond to the reversible deintercalation of $Al^{3+}$ and the oxidation of $Mn^{2+}$ within the $Al_xMnO_2$ structure. To gain deeper insights into the charge/discharge mechanism, *ex situ* XRD measurements were conducted at various electrochemical states throughout the charging and discharging process. As shown in Figure S24, a noticeable change in the intensity of a characteristic peak around 25°, corresponding to the (210) plane of MnOOH, was observed during the discharge/charge process.[48] The peak intensity increases significantly as the battery is discharged to 0.9 V, but gradually weakens and disappears during further discharge. This suggests that $H^+$ insertion occurs at the first discharge plateau (1.4–1.0 V), and the MnOOH formed during this process decomposes upon further discharge.[50] This electrochemical response underscores the robust and reversible nature of $H^+$ and $Al^{3+}$ co-intercalation and Mn redox reactions in the $Al_xMnO_2$ cathode.

Figure 5b illustrates the characteristic voltage curves of Al//AE//$Al_xMnO_2$ and Al//HE//$Al_xMnO_2$ cells under a current density of 0.1 $A\,g^{-1}$, with the voltage plateaus in accordance with the redox peaks depicted in the CV curves. Due to the optimization of Al stripping/plating performance in the HE electrolyte, the full cells are superior to AE at various discharge/charge rates. As depicted in Figure 5c, the Al//HE//$Al_xMnO_2$ battery achieves a specific capacity of approximately ~400 $mAh\,g^{-1}$ based on $Al_xMnO_2$ mass. As the current density increases to 2 $A\,g^{-1}$, the specific of the Al//HE//$Al_xMnO_2$ battery can still maintain a discharge capacity of 175 $mAh\,g^{-1}$, implying the excellent rate capability of HE. The long-term cycle stability of the battery was tested by galvanostatic charge/discharge (GCD) with a current density of 0.3 $A\,g^{-1}$ (Figure 5d). The full cell using HE electrolyte can maintain a much longer cycling lifespan and prefer stability (223 $mAh\,g^{-1}$ retention after 400 cycles at 0.3 $A\,g^{-1}$) than those using AE electrolyte. The low cycle stability of AE can be attributed to the irreversibility problem of metallic aluminum, that is, hydrogen evolution reaction caused by side reactions and hydrogen evolution leading to electrode contact problems. The electrochemical performance of Al//HE//$Al_xMnO_2$, including initial specific capacity, rate capability, discharge potential, cycle number, and capacity retention, is summarized in Table S1, which demonstrates that the electrochemical performance of the assembled Al//HE//$Al_xMnO_2$ is exceptional among the AAIBs reported to date.

Electrochemical impedance spectroscopy (EIS) analysis further verified the expectation that high-polarity DMF/DMMP optimizes Al stripping/plating kinetics. The resultant EIS spectra have been fitted according to the Randles equivalent circuit, consisting of high-frequency depressed semicircles and low-frequency linear tails (Figure 5e and Figure S25). The $R_{ct}$ value of HE is significantly lower than that of AE (317.5 Ω vs. 627.3 Ω), which proves the superiority of HE electrolyte again. Moreover, as depicted in Figure 5f, the SEM image illustrates that the surface of the Al anode, subjected to irregular Al corrosion in AE, appears rough and porous after 100 cycles at 0.3 $A\,g^{-1}$. In stark contrast, a uniformly flat surface, characterized by densely deposited Al, is observed under same conditions in HE (Figure 5g). Elevated water proton-electron density in the electrolyte empowers Al–Mn batteries with exceptional cycle life, high efficiency, and effective capacity utilization due to its distinctive water retention capacity, offers valuable insights for designing electrolytes in AAIBs.

## Conclusions

The efficient and cost-effective additive, DMF and DMMP, is introduced into the typical $Al(OTf)_3$ electrolyte to effectively suppress solvation reaction in AAIBs. In the composite electrolyte (HE), the interaction with polar DMF and DMMP molecules is employed to augment the electron density on water protons, diminishing the thermodynamic favorability of $H_2O$ dissociation. Ultimately, this fortifies the O–H bonds within water molecules. Simultaneously, the flammability and Al corrosion in the hybrid electrolyte is mitigated, leading to an extension of the electrochemical stability window and security of the electrolyte. As a proof of concept, the distinctive solvation structure and robust interaction between DMF/DMMP and $H_2O$ serve to diminish the size of hydrated $Al^{3+}$ that preserves the structural stability of $Al_xMnO_2$ to delivers a high specific capacity of 235 $mAh\,g^{-1}$ for 400 cycles. The findings are poised to introduce novel insights into the practical design of highly reversible aqueous aluminum ion batteries, and the substantial practical value is anticipated to generate widespread interest among researchers and manufacturers.

## Acknowledgements

X.Y. acknowledge the support from National Sciences Foundation of China (51971065) and the Innovation Program of Shanghai Municipal Education Commission (2019-01-07-00-07-E00028).

## Conflict of Interest

The authors declare no conflict of interest.

## Data Availability Statement

The data that support the findings of this study are available from the corresponding author upon reasonable request.

**Keywords:** aqueous electrolytes · electrolyte decomposition · hybrid electrolyte engineering · highly reversible aqueous aluminum ion batteries


[1] C. Wu, S. Gu, Q. Zhang, Y. Bai, M. Li, Y. Yuan, H. Wang, X. Liu, Y. Yuan, N. Zhu, F. Wu, H. Li, L. Gu, J. Lu, *Nat. Commun.* **2019**, *10*.

[2] C. Yan, C. Lv, B. E. Jia, L. Zhong, X. Cao, X. Guo, H. Liu, W. Xu, D. Liu, L. Yang, J. Liu, H. H. Hng, W. Chen, L. Song, S. Li, Z. Liu, Q. Yan, G. Yu, *J. Am. Chem. Soc.* **2022**, *144*, 11444–11455.

[3] B. E. Jia, A. Q. Thang, C. Yan, C. Liu, C. Lv, Q. Zhu, J. Xu, J. Chen, H. Pan, Q. Yan, *Small* **2022**, *18*, e2107773.

[4] W. Lv, G. Wu, X. Li, J. Li, Z. Li, *Energy Storage Mater.* **2022**, *46*, 138–146.

[5] X. Yang, H. Gu, Q. Sun, W. Zhang, Z. Li, *Energy Storage Mater.* **2023**, *61*, 102917.

[6] C. Yan, C. Lv, L. Wang, W. Cui, L. Zhang, K. N. Dinh, H. Tan, C. Wu, T. Wu, Y. Ren, J. Chen, Z. Liu, M. Srinivasan, X. Rui, Q. Yan, G. Yu, *J. Am. Chem. Soc.* **2020**, *142*, 15295–15304.

[7] Q. Ran, H. Shi, H. Meng, S. P. Zeng, W. B. Wan, W. Zhang, Z. Wen, X. Y. Lang, Q. Jiang, *Nat. Commun.* **2022**, *13*, 576.

[8] T. Zhang, Y. Tang, S. Guo, X. Cao, A. Pan, G. Fang, J. Zhou, S. Liang, *Energy Environ. Sci.* **2020**, *13*, 4625–4665.

[9] J. Hao, L. Yuan, C. Ye, D. Chao, K. Davey, Z. Guo, S. Z. Qiao, *Angew. Chem. Int. Ed.* **2021**, *60*, 7366–7375.

[10] P. Wang, Z. Chen, H. Wang, Z. Ji, Y. Feng, J. Wang, J. Liu, M. Hu, J. Fei, W. Gan, Y. Huang, *Energy Storage Mater.* **2020**, *25*, 426–435.

[11] J. Yang, W. Gong, F. Geng, *Adv. Funct. Mater.* **2023**, *33*.

[12] Y. Wang, T. Wu, H. Gu, W. Zhang, Z. Li, *Energy Storage Mater.* **2024**, *70*, 103488.

[13] C. Hu, Y. Lu, H. Gu, W. Zhang, Z. Li, *ACS Energy Lett.* **2024**, *9*, 4353–4360.

[14] X. Shi, J. Xie, J. Wang, S. Xie, Z. Yang, X. Lu, *Nat. Commun.* **2024**, *15*, 302.

[15] Y. Wang, Z. Wang, W. K. Pang, W. Lie, J. A. Yuwono, G. Liang, S. Liu, A. M. Angelo, J. Deng, Y. Fan, K. Davey, B. Li, Z. Guo, *Nat. Commun.* **2023**, *14*, 2720.

[16] F. Wang, O. Borodin, T. Gao, X. Fan, W. Sun, F. Han, A. Faraone, J. A. Dura, K. Xu, C. Wang, *Nat. Mater.* **2018**, *17*, 543–549.

[17] A. Nimkar, K. Alam, G. Bergman, M. D. Levi, D. T. Major, N. Shpigel, D. Aurbach, *Angew. Chem. Int. Ed.* **2023**, *62*, e202311373.

[18] G. R. Pastel, Y. Chen, T. P. Pollard, M. A. Schroeder, M. E. Bowden, A. Zheng, N. T. Hahn, L. Ma, V. Murugesan, J. Ho, M. Garaga, O. Borodin, K. Mueller, S. Greenbaum, K. Xu, *Energy Environ. Sci.* **2022**, *15*, 2460–2469.

[19] Z. Zhao, Z. Zhang, T. Xu, W. Wang, B. Wang, X. Yu, *J. Am. Chem. Soc.* **2024**, *146*, 2257–2266.

[20] G. Ma, S. Di, Y. Wang, W. Yuan, X. Ji, K. Qiu, M. Liu, X. Nie, N. Zhang, *Energy Storage Mater.* **2023**, *54*, 276–283.

[21] T. C. Li, Y. Lim, X. L. Li, S. Luo, C. Lin, D. Fang, S. Xia, Y. Wang, H. Y. Yang, *Adv. Energy Mater.* **2022**, *12*, 2103231.

[22] F. Ming, Y. Zhu, G. Huang, A. H. Emwas, H. Liang, Y. Cui, H. N. Alshareef, *J. Am. Chem. Soc.* **2022**, *144*, 7160–7170.

[23] L. Miao, R. Wang, S. Di, Z. Qian, L. Zhang, W. Xin, M. Liu, Z. Zhu, S. Chu, Y. Du, N. Zhang, *ACS Nano* **2022**, *16*, 9667–9678.

[24] N. Chang, T. Li, R. Li, S. Wang, Y. Yin, H. Zhang, X. Li, *Energy Environ. Sci.* **2020**, *13*, 3527–3535.

[25] S. Hess, M. Wohlfahrt-Mehrens, M. Wachtler, *J. Electrochem. Soc.* **2015**, *162*, A3084–A3097.

[26] X. Yuan, Y. Li, Y. Zhu, W. Deng, C. Li, Z. Zhou, J. Hu, M. Zhang, H. Chen, R. Li, *ACS Appl. Mater. Interfaces* **2021**, *13*, 38248–38255.

[27] Q. Zhang, Y. Ma, Y. Lu, X. Zhou, L. Lin, L. Li, Z. Yan, Q. Zhao, K. Zhang, J. Chen, *Angew. Chem. Int. Ed.* **2021**, *60*, 23357–23364.

[28] Y. Li, X. Wei, L. Chen, J. Shi, *Angew. Chem. Int. Ed.* **2021**, *60*, 19550–19571.

[29] X. Yang, C. Zhang, L. Chai, W. Zhang, Z. Li, *Adv. Mater.* **2022**, *34*, e2206099.

[30] Y. Li, L. Liu, Y. Lu, R. Shi, Y. Ma, Z. Yan, K. Zhang, J. Chen, *Adv. Funct. Mater.* **2021**, *31*, 2102063.

[31] Y. Miao, H. Yan, X. Qiu, X. Zhou, D. Zhu, X. Li, T. Qiu, *Appl. Clay Sci.* **2022**, *223*, 106498.

[32] M. Druchok, M. Holovko, T. Bryk, *Condens. Matter Phys.* **2004**.

[33] J. M. Ruiz, M. H. McAdon, J. M. Garces, *J. Phys. Chem. B* **1997**, *101*, 1733–1744.

[34] J. A. Aguilar, S. Faulkner, M. Nilsson, G. A. Morris, *Angew. Chem. Int. Ed.* **2010**, *49*, 3901–3903.

[35] J. McAllister, N. A. G. Bandeira, J. C. McGlynn, A. Y. Ganin, Y. F. Song, C. Bo, H. N. Miras, *Nat. Commun.* **2019**, *10*, 370.

[36] Y. J. Chang, E. W. Castner Jr, *J. Chem. Phys.* **1993**, *99*, 113–125.

[37] Z. Song, L. Miao, H. Duan, L. Ruhlmann, Y. Lv, D. Zhu, L. Li, L. Gan, M. Liu, *Angew. Chem. Int. Ed.* **2022**, *61*, e202208821.

[38] L. Suo, O. Borodin, Y. Wang, X. Rong, W. Sun, X. Fan, S. Xu, M. A. Schroeder, A. V. Cresce, F. Wang, C. Yang, Y. S. Hu, K. Xu, C. Wang, *Adv. Energy Mater.* **2017**, *7*, 1701189.

[39] J. Yang, R. Dettori, J. P. F. Nunes, N. H. List, E. Biasin, M. Centurion, Z. Chen, A. A. Cordones, D. P. Deponte, T. F. Heinz, M. E. Kozina, K. Ledbetter, M. F. Lin, A. M. Lindenberg, M. Mo, A. Nilsson, X. Shen, T. J. A. Wolf, D. Donadio, K. J. Gaffney, T. J. Martinez, X. Wang, *Nature* **2021**, *596*, 531–535.

[40] P. Sun, L. Ma, W. Zhou, M. Qiu, Z. Wang, D. Chao, W. Mai, *Angew. Chem. Int. Ed.* **2021**, *60*, 18247–18255.

[41] Z. Liu, R. Wang, Y. Gao, S. Zhang, J. Wan, J. Mao, L. Zhang, H. Li, J. Hao, G. Li, L. Zhang, C. Zhang, *Adv. Funct. Mater.* **2023**, *33*, 2308463.

[42] J. Sicklinger, H. Beyer, L. Hartmann, F. Riewald, C. Sedlmeier, H. A. Gasteiger, *J. Electrochem. Soc.* **2020**, *167*, 130507.

[43] H. L. Hsu, K. R. Leong, I. J. Teng, M. Halamicek, J. Y. Juang, S. R. Jian, L. Qian, N. P. Kherani, *Materials (Basel)* **2014**, *7*, 5643–5663.

[44] J. Zhou, F. Qi, Y. Chen, Z. Wang, B. Zheng, X. Wang, *J. Mater. Sci.* **2018**, *53*, 7767–7777.

[45] G. A. Novak, M. P. Vermeuel, T. H. Bertram, *Atmospheric Measurement Techniques* **2020**, *13*, 1887–1907.

[46] D. Liu, I. T. Martin, J. Zhou, E. R. Fisher, *Pure Appl. Chem.* **2006**, *78*, 1187–1202.

[47] K. Marciszuk, T. Pieńkos, P. Gontarz, A. Pelc, *ChemPhysChem* **2020**, *21*, 1695–1702.

[48] X. Yang, C. Zhang, L. Chai, W. Zhang, Z. Li, *Adv. Mater.* **2022**, *34*, 2206099.

[49] H. Gu, X. Yang, S. Chen, W. Zhang, H. Y. Yang, Z. Li, *Nano Lett.* **2023**, *23*, 11842–11849.

[50] X. Yang, H. Gu, L. Chai, S. Chen, W. Zhang, H. Y. Yang, Z. Li, *Nano Lett.* **2024**, *24*, 8542–8549.


Manuscript received: August 13, 2024
Accepted manuscript online: October 17, 2024
Version of record online: November 13, 2024